

Experimental and Theoretical Studies of Serpentine Interconnects on Ultrathin Elastomers for Stretchable Electronics

Taisong Pan, Matt Pharr, Yinji Ma, Rui Ning, Zheng Yan, Renxiao Xu, Xue Feng, Yonggang Huang, and John A. Rogers*

Integrating deformable interconnects with inorganic functional materials establishes a path to high-performance stretchable electronics. A number of applications demand that these systems sustain large deformations under repetitive loading. In this manuscript, the influence of the elastomeric substrate on the stretchability of serpentine interconnects is investigated theoretically and experimentally. Finite element analyses (FEA) reveal a substantial increase in the elastic stretchability with reductions in substrate thickness. Low-cycle fatigue tests confirm this trend by examining the stretch required to form fatigue cracks associated with plastic deformation. To elucidate the mechanics governing this phenomenon, the buckling behaviors of deformed serpentine interconnects on substrates of various thicknesses are examined. The analytical model and FEA simulations suggest a change in the buckling mode from local wrinkling to global buckling below a critical thickness of the substrate. Scanning electron microscope and 3D optical profiler studies verify this transition in buckling behavior. The global buckling found in thin substrates accommodates large stretching prior to plastic deformation of the serpentine, thereby drastically enhancing the stretchability of these systems.

1. Introduction

Integrations of high-performance inorganic semiconductors with soft elastomeric substrates establish the foundations for classes of electronic devices that can stretch, twist, and bend,^[1–6] enabling applications in wearable electronics,^[5,7–10] optogenetics,^[11] artificial skins,^[12–16] and many other areas. Stretchability in these systems can be achieved via an “island-bridge” layout in which conductive traces (bridges) interconnect the rigid, functional components (islands).^[17–19] The conductive interconnects must have low effective stiffness to accommodate stretching/deformation, thereby isolating functional components from strains and allowing invariant functionality and mechanical integrity.

Serpentine layouts in the interconnects,^[20–27] typically of periodic arcs and straight segments, can offer levels of

Dr. T. Pan
State Key Laboratory of Electronic Thin Films and Integrated Devices
University of Electronic Science and Technology of China
Chengdu 610054, China

Dr. T. Pan
Department of Civil and Environmental Engineering
Northwestern University
Evanston, IL 60208, USA

Prof. M. Pharr
Department of Mechanical Engineering
Texas A&M University
College Station, TX 77843, USA

Dr. Y. Ma, Prof. Y. Huang
Department of Civil and Environmental Engineering, Mechanical
Engineering, and Materials Science and Engineering
Northwestern University
Evanston, IL 60208, USA

Dr. Y. Ma, Prof. X. Feng
AML
Department of Engineering Mechanics
Center for Mechanics and Materials
Tsinghua University
Beijing 100084, China

R. Ning, Dr. Z. Yan
Department of Materials Science and Engineering
Frederick Seitz Materials Research Laboratory
University of Illinois at Urbana-Champaign
Urbana, IL 61801, USA

R. Xu
Department of Civil and Environmental Engineering
and Mechanical Engineering
Northwestern University
Evanston, IL 60208, USA

Prof. J. A. Rogers
Departments of Materials Science and Engineering
Biomedical Engineering, Chemistry, Mechanical Engineering, Electrical
Engineering and Computer Science
Center for Bio-Integrated Electronics
Simpson Querrey Institute for Nano/biotechnology
Northwestern University
Evanston, IL 60208, USA
E-mail: jrogers@northwestern.edu

 The ORCID identification number(s) for the author(s) of this article can be found under <https://doi.org/10.1002/adfm.201702589>.

DOI: 10.1002/adfm.201702589

stretchability that meet requirements for many applications. In many of these designs, the serpentines fully bond to the elastomeric substrate to prevent damage from external physical contact.^[17,28–32] Additionally, across the wide range of examples of this design, the substrate material type and thickness can vary significantly.^[33–36] As a result, the interplay between substrate properties and deformation of the interconnects is critical. In particular, mechanical properties such as tensile stiffness and bending stiffness depend on the thickness and elastic modulus of the substrate, and these properties can strongly influence the behavior of the interconnects.

This manuscript investigates the influence of substrate stiffness (modulus and thickness) on the mechanical performance of serpentine interconnects through combined finite element analyses (FEA), analytical modeling, and experiments. We identify the key mechanics that enable large deformation of interconnects on ultrathin substrates. We also uncover distinct buckling modes that facilitate stretching and specify conditions under which these buckling modes occur. Overall, we provide experimental and theoretical results that can guide the design of high-performance electronic devices with extreme stretchability.

2. Results and Discussions

Figure 1a shows the basic fabrication approach employed in this study. Photolithography produced metallic serpentine interconnects encapsulated above and below by a stiff polymer (polyimide, PI). Transfer printing to a silicone substrate yielded the final structures. Stretching of the substrate allowed for investigation of the deformation behavior of the interconnects. Figure 1b provides geometric details of the serpentines, which consist of several periodic unit cells of two straight lines and two semicircles. In our studies, we fixed the dimensions and materials of the serpentines to focus on the influence of the substrate on the deformation behavior. The widths of the interconnects are $w = 40 \mu\text{m}$, the lengths of the straight segments are $l_1 = 420 \mu\text{m}$, and the inner diameters of the semicircles are $l_2 = 140 \mu\text{m}$. Through the thickness, the serpentine interconnect has a layered structure (Figure 1b) from bottom (interface of serpentine/substrate) to top of 30 nm SiO_2 /3 nm Ti/1.2 μm PI/100 nm Cu/1.2 μm PI. The Ti and SiO_2 layers provide adhesion to the silicone substrates. Figure 1c shows scanning electron microscope (SEM) images of interconnects on a silicone substrate (Ecoflex 00-30) before and after 100% stretching, and indicates strong bonding between the two.

To study the influence of the substrate thickness on the stretchability, we performed FEA and cyclic loading experiments with a focus on the elastic stretchability, defined as the applied strain at the onset of plastic deformation in the interconnect. In FEA, we determined the elastic stretchability by setting the maximum principal strain equal to the yield strain (for copper, $\approx 0.3\%$).^[31,37] Figure 2a shows the elastic stretchability of the interconnect versus the substrate thickness for substrates made of two different formulations of silicone polymer, Ecoflex and Sylgard 184. For both materials, the elastic stretchability of the interconnect increases significantly

with decreasing substrate thickness within a certain range. A comparison of the results suggests that the stretchability also increases with decreasing elastic modulus of the substrate ($E_{\text{Ecoflex}} = 60 \text{ kPa}$ and $E_{\text{Sylgard}} = 1 \text{ MPa}$). To validate these FEA findings, we conducted cyclic loading experiments of serpentine interconnects on substrates of varying thickness. A cyclic loader subjected the samples to 25 000 loading cycles at 5 Hz at strain levels indicated in Figure 2a. After these experiments, we examined the samples in an optical microscope to inspect for microcracks in the interconnects. As an example, Figure 2b shows that subjecting a 7 μm Ecoflex substrate to a strain of 120% for 25 000 cycles failed to form observable microcracks. By comparison, stretching a 7 μm Ecoflex substrate to a strain of 140% for the same number of cycles yielded visible microcracks in the semicircular regions. We observed no microcracks after a single loading at either strain level. In other words, we believe that microcracks result from repetitive loading into the plastic regime, i.e., they are due to fatigue. The left panel of Figure 2b provides the strain distribution in the semicircular regions at the onset of plastic deformation for 7 μm thick Ecoflex and 700 μm thick Sylgard 184 substrates. Figure S1 in the Supporting Information shows the strain distribution for other substrate thicknesses. All of these simulations suggest that the maximum strain occurs on the inner edge (top edge in Figure 2b, left panel) of the semicircular regions, consistent with experimental observations in the right panel of Figure 2b, which suggest that fatigue cracks initiate from these locations. The experimental investigations shown in Figure 2b allowed for construction of Figure 2a. The “x” symbols indicate experiments in which we observed fatigue cracks while the “o” symbols represent experiments in which we did not observe any such cracks. The experiments show good agreement with the predictions from FEA, thus demonstrating the utility of FEA in investigating the influence of the substrate on the deformation and failure characteristics of the interconnects. Figure 2a also shows that the elastic stretchability does not change substantially with substrate thickness for thicknesses larger than $\approx 100 \mu\text{m}$. In other words, the dependence of the elastic stretchability on the substrate thickness exhibits a two-stage, nonlinear behavior, implying different mechanisms in each stage.

We now establish plane-strain analytical models to identify the aforementioned mechanisms of deformation for thin and thick substrates. We first obtain the effective plane-strain modulus and thickness of the multilayer serpentine interconnect. The effective bending stiffness EI of the layered structure (five layers, Figure 1b) of the interconnect is given by^[38]

$$EI = \sum_{i=1}^5 \bar{E}_i h_i \left\{ \frac{h_i^2}{3} + \left[\left(\sum_{j=1}^i h_j \right) - h_{\text{neutral}} \right]^2 - h_i \left[\left(\sum_{j=1}^i h_j \right) - h_{\text{neutral}} \right] \right\}, \quad (1)$$

where the plane-strain modulus of i th layer $\bar{E}_i = E_i / (1 - \nu_i^2)$ is related to its elastic modulus E_i and Poisson's ratio ν_i , and h_i is thickness of i th layer. The distance h_{neutral} from the neutral mechanical plane to the bottom of the cross section is given by

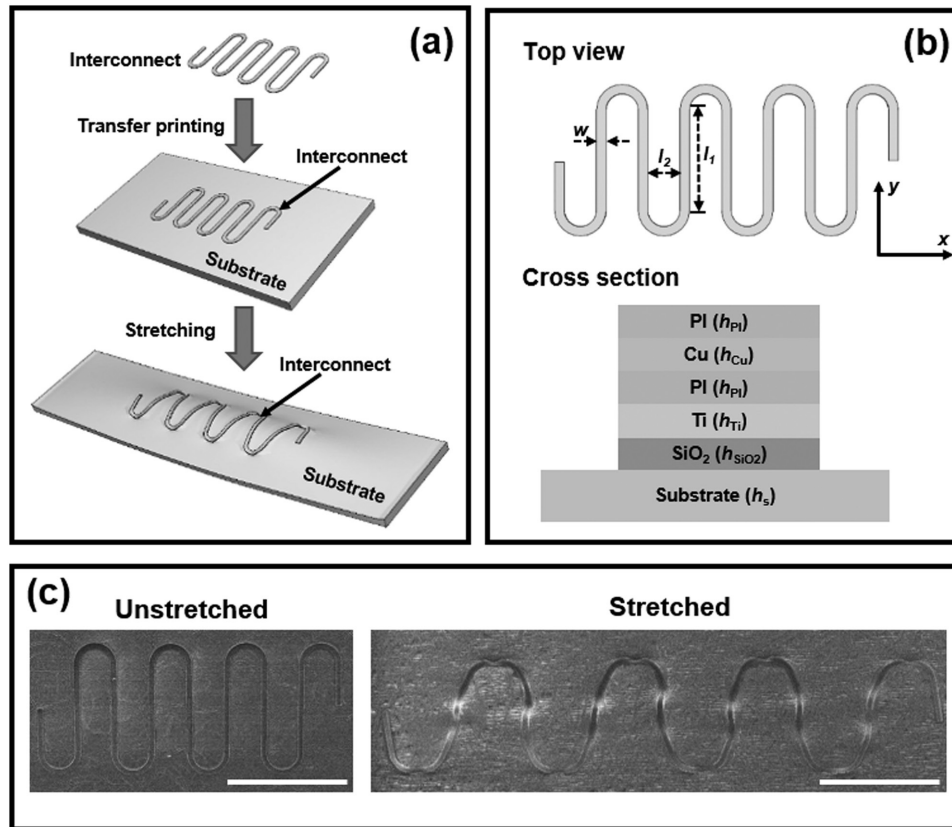


Figure 1. a) Illustration of the steps for fabricating a serpentine interconnect on a soft substrate. b) Geometric layout of the serpentine interconnect. c) SEM images of the serpentine interconnects on a 500 μm thick Ecoflex substrate in the unstretched state (left) and at 100% applied strain (right). The scale bar represents 500 μm .

$$h_{\text{neutral}} = \frac{\sum_{i=1}^5 \bar{E}_i h_i \left[\left(\sum_{j=1}^i h_j \right) - \frac{h_i}{2} \right]}{\sum_{i=1}^5 \bar{E}_i h_i} \quad (2)$$

The effective thickness h_f and the effective plane-strain modulus \bar{E}_f of the interconnect are defined by^[39]

$$h_f = \sqrt{\frac{12EI}{\sum_{i=1}^5 \bar{E}_i h_i}} \quad (3)$$

$$\bar{E}_f = \frac{\sum_{i=1}^5 \bar{E}_i h_i}{h_f} \quad (4)$$

They are 1.9 μm and 11.76 GPa for the interconnects shown in Figure 1b and the elastic properties given in the Supporting Information.

Due to the Poisson effect, the vertically aligned straight segments (arms) of the interconnect undergo compression in the vertical direction (y -direction in Figure 1b) when stretching the substrate in the horizontal direction (x -direction in Figure 1b). The straight segment of the serpentine interconnect can be modeled as a compressed thin, stiff ribbon on a compliant substrate, for which Wang et al. reported different buckling modes

at different levels of compressive strains.^[40] These buckling modes are separated by a critical length l_{cr} , given by

$$l_{\text{cr}} = 4\pi \sqrt{\frac{\bar{E}I}{\bar{E}_f h_f + \bar{E}_s h_s} \left\{ \frac{\left[\frac{\bar{E}_f}{3\bar{E}_s} \right]^{2/3}}{G_s (h_f + h_s)} - 0.3 \right\}} \quad (5)$$

where the plane-strain modulus of the substrate $\bar{E}_s = E_s/(1-\nu_s^2)$ is related to its elastic modulus E_s and Poisson's ratio ν_s ; $G_s = E_s/[2(1+\nu_s)]$ is the shear modulus; h_s is the substrate thickness; \bar{E}_f is the effective plane-strain modulus of serpentine interconnect given in Equation (4); and the effective bending stiffness of the entire interconnect/substrate system $\bar{E}I$ is given by

$$\bar{E}I = \frac{(\bar{E}_f h_s^2 - \bar{E}_s h_s^2)^2 + 4\bar{E}_f h_f \bar{E}_s h_s (h_f + h_s)^2}{12(\bar{E}_f h_f + \bar{E}_s h_s)} \quad (6)$$

Global buckling (each straight segment of the serpentine interconnect forming a single, large buckle; Figure S2, Supporting Information) occurs when the length l_1 of the straight segment of the serpentine (Figure 1b) is larger than l_{cr} . For l_1 smaller than l_{cr} , local wrinkling occurs, i.e., multiple small buckles form (Figure S3, Supporting Information). The change

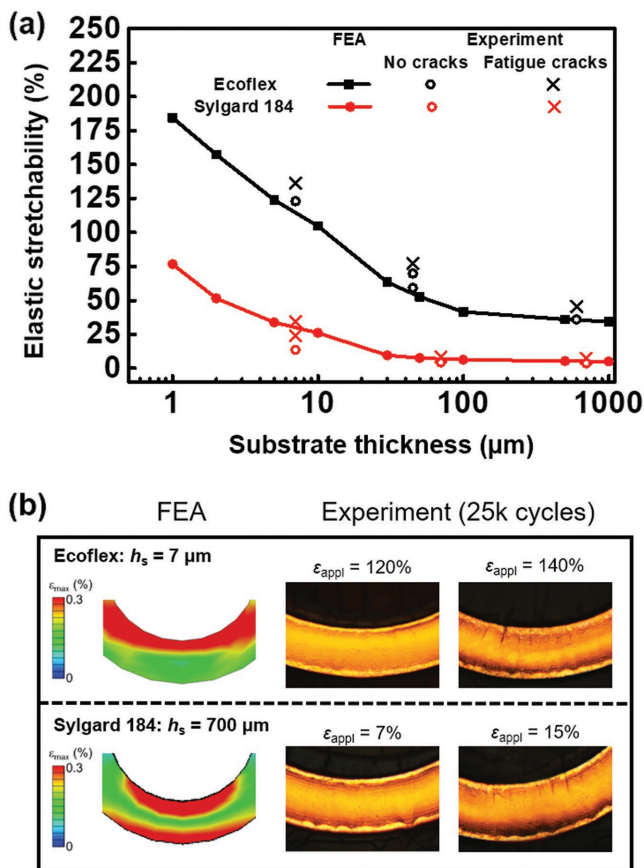


Figure 2. a) FEA and experimental results of the elastic stretchability as a function of substrate thickness. b) FEA results of the strain distribution (ϵ_{\max}) in the copper layer of serpentine interconnects near the semicircular, high-strain region at the onset of plastic deformation (left panel), and optical images near the same region after 25 000 cycles (right panel) for various levels of stretch (ϵ_{appl}).

of buckling mode can be achieved by adjusting l_{cr} via the substrate thickness (h_s) or via the length of straight segment (l_1) of the serpentine interconnect.

The buckling modes governed by the critical length l_{cr} in Equation (5) are compared with SEM images of stretched interconnects. The solid black curve in **Figure 3a** indicates the critical condition separating global and local buckling ($l_1 = l_{\text{cr}}$) versus the substrate thickness (h_s), both nondimensionalized by the effective thickness of the interconnect (h_f). A length of the straight segment, l_1 , above (or to the left of) the solid black curve will result in global buckling of the interconnects, while a length of the straight segment, l_1 , below (or to the right of) the curve will result in local wrinkling of the interconnects. By setting the critical length l_{cr} equal to the length of straight segment used in the experiments ($l_1 = 420 \mu\text{m}$), the analytic model discussed above predicts local wrinkling for an Ecoflex substrate thicker than $218 \mu\text{m}$, or a Sylgard 184 substrate thicker than $100 \mu\text{m}$. These numbers are consistent with the SEM images in **Figure 3b**, which clearly show local wrinkling of the straight segments of the interconnects for $750 \mu\text{m}$ thick Sylgard 184 and $500 \mu\text{m}$ thick Ecoflex substrates. Likewise, **Figure 3b** indicates global buckling of the interconnects on both $11 \mu\text{m}$

thick Sylgard 184 and $11 \mu\text{m}$ thick Ecoflex substrates, which are thinner than the critical thicknesses predicted in the analytical model. For a length of the straight segment l_1 very close to l_{cr} , the FEA results suggest a mixed buckling mode, in which global buckling and local wrinkling coexist. The Supporting Information (Figures S2–S5, Supporting Information) provides additional detailed comparisons of the buckling modes of serpentine interconnects on substrates of different thicknesses.

To further quantify this buckling behavior, we measured the deformation of serpentine interconnects using a 3D optical profiler. **Figure 4a** shows such data on the out-of-plane deformation of a serpentine interconnect on stretched 11 and $750 \mu\text{m}$ thick Sylgard 184 substrates. These measurements agree well with the results obtained by FEA in **Figure 4b**. **Figure 4c** further compares the experimental and numerical results of the out-of-plane displacement for a line scan along the dashed white lines in **Figure 4a,b**. For the $11 \mu\text{m}$ thick Sylgard 184 substrate, both FEA and experiments indicate global buckling of the interconnect (forming a single buckle along each straight segment of the interconnect). Moreover, the predicted and measured amplitudes of the buckle are consistent (left panel of **Figure 4c**). For the $750 \mu\text{m}$ thick Sylgard 184 substrate, both FEA and experiments indicate local wrinkling of the interconnect (forming multiple buckles along each straight segment of the interconnect), and their amplitude and wavelength are also quite consistent (right panel of **Figure 4c**). We also compared the buckle wavelength λ in local wrinkling obtained by experiments and FEA to a new analytical model developed in this manuscript that accounts for the effects of finite width^[41] and finite deformation^[42]

$$\lambda = \frac{2\pi h_f \left(\frac{\bar{E}_f}{3\bar{E}_s} \right)^{1/3}}{1 + \epsilon_y} \tanh \left\{ \frac{16}{15} \left[\left(\frac{\bar{E}_s}{\bar{E}_f} \right)^{1/3} \frac{w}{h_f} \right]^{1/4} \right\} \quad (7)$$

where w is the width of serpentine interconnect and ϵ_y is the vertical strain (y -direction in **Figure 1b**) due to the Poisson's effect, which is related to the applied strain ϵ_x in the horizontal direction (x -direction in **Figure 1b**) by $\ln(1 - \epsilon_y) = -0.5 \ln(1 + \epsilon_x)$. For the serpentine used in the experiments on a $750 \mu\text{m}$ thick Sylgard 184 substrate under 30% applied strain, Equation (7) predicts a wavelength of $123 \mu\text{m}$, which can be compared to $128 \mu\text{m}$ from FEA and $97 \mu\text{m}$ from the experiments. Similarly, for a $500 \mu\text{m}$ thick Ecoflex substrate under 100% applied strain (**Figure S6**, Supporting Information), Equation (7) predicts a wavelength of $238 \mu\text{m}$, which can be compared to $233 \mu\text{m}$ from FEA and $200 \mu\text{m}$ from the experiments. Overall, the analytical model produces excellent agreement with the FEA results and experiments.

This analysis of buckling modes provides insight into the two-stage, nonlinear relationship found between the substrate thickness and the elastic stretchability of serpentine interconnects (**Figure 2a**). Both theory and experiments suggest a critical length, l_{cr} , of the straight segment of the serpentine, below which the serpentine exhibits local wrinkling and above which they exhibit global buckling. The substrate thickness influences this critical length (Equation (5)). For a fixed serpentine geometry, when the substrate is thick enough to induce the local

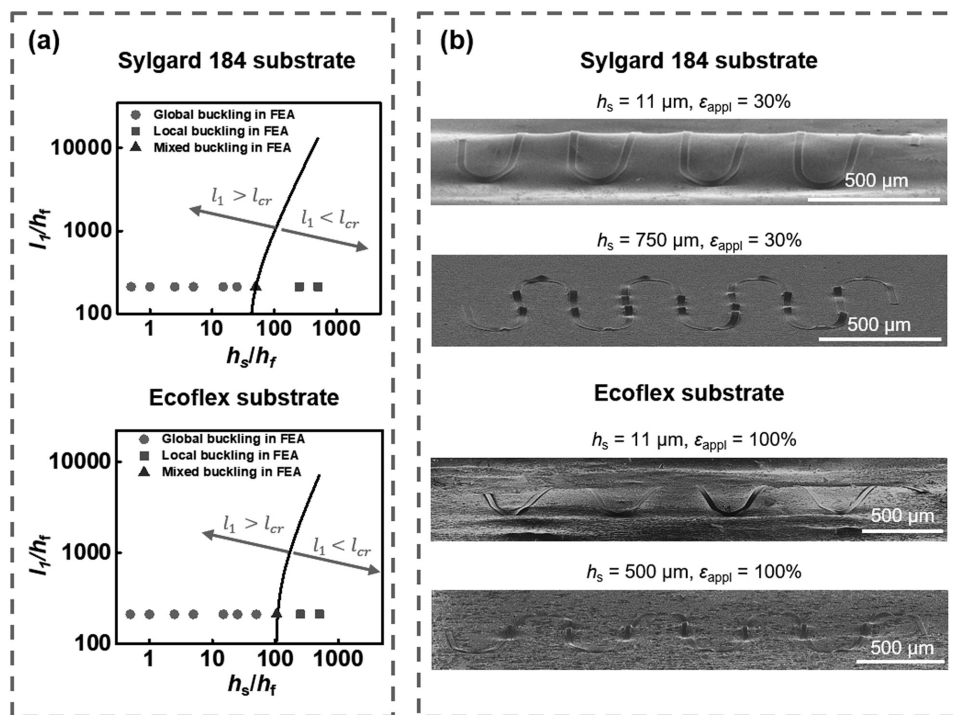


Figure 3. a) Buckling modes obtained by FEA. The solid black curve indicates the normalized critical condition ($l_1 = l_{cr}$) separating global and local buckling as a function of the normalized substrate thickness (h_s/h_f). b) Angled-view SEM images of deformed serpentine interconnects with different substrate materials and thicknesses. ϵ_{appl} is the applied strain.

wrinkling mode, $l_1 < l_{cr}$, the serpentine interconnect becomes insensitive to the substrate thickness. By comparison, as the substrate thickness reduces such that $l_1 > l_{cr}$, global buckling occurs. Compared to local wrinkling, global buckling produces a larger buckling amplitude (Figure 4c). The larger buckling amplitude allows the semicircles of the interconnects to buckle out of plane (downward in the thickness direction), as opposed to in-plane stretching, thereby reducing the strain concentrations in the semicircles. As a result, more stretching of the substrate can be accommodated prior to plastic deformation in interconnects that exhibit global buckling, i.e., they exhibit larger elastic stretchability. Likewise, for interconnects that exhibit global buckling, even thinner substrates allow for even larger buckle amplitudes. In summary, global buckling occurs for $l_1 > l_{cr}$, and the elastic stretchability increases significantly with decreasing substrate thickness.

The elastic stretchability can be further increased by optimizing the substrate material and/or metal for the interconnect. As shown in Figure 5a, for a 100 nm thick metal layer on a 5 μm thick substrate, the elastic stretchability increases substantially as the elastic modulus of the interconnect decreases. This phenomenon occurs because the effective bending stiffness of the combined interconnect and substrate system decreases with the elastic modulus of the interconnect. As a result, the entire structure of the interconnect and substrate can buckle out of plane, thus reducing strains in the semicircular regions of the interconnect. We note that this relation between elastic modulus of interconnect and its elastic stretchability would be different for a much thicker substrate. For instance, for a 1 μm thick metal layer on a 1 mm thick Ecoflex substrate,

Zhang et al. reported a weak dependence of the elastic stretchability on the elastic modulus of the interconnect (for substrates with no prestretch, as in this study).^[22] This trend likely results from the relative inability of thick films on thick substrates to buckle at all. Instead, stretching of the interconnects results in in-plane bending/stretching of the semicircular regions, which depend only weakly on the elastic modulus of the metal. Additionally, the elastic stretchability of interconnect correlates strongly with the elastic modulus of substrate. As shown in Figure 5b, the elastic stretchability increases substantially as the elastic modulus of the substrate decreases.

3. Conclusions

This paper investigates the influence of the substrate on the stretchability of serpentine interconnects in stretchable electronic systems. Experimental and theoretical studies indicate a drastic increase in the stretchability with decreasing substrate thickness. However, this relationship is nonlinear: the elastic stretchability rapidly increases only below a critical thickness of the substrate. By comparison, when the substrate is thick, the elastic stretchability of the interconnects only weakly depends on the substrate thickness. To study the mechanics that dictate this behavior, we examine the buckling modes of stretched serpentine through analytical modeling, FEA simulations, and experimental studies. We identify a critical length, l_{cr} , that governs a transition from local wrinkling to global buckling with reducing substrate thickness. Global buckling of thin substrates enables increased stretching before plastic deformation

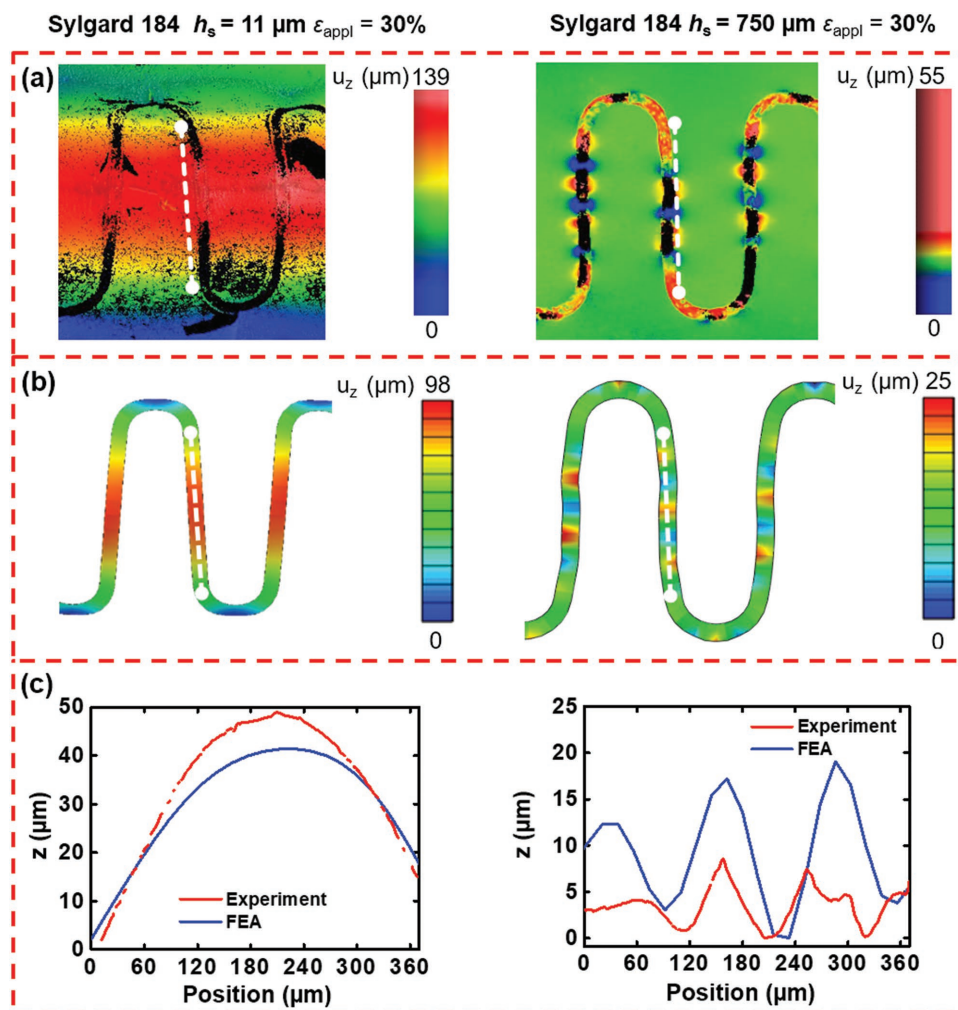


Figure 4. a) Experimental 3D optical profiles showing the out-of-plane displacement (u_z) of a serpentine interconnect on 11 μm (left) and 750 μm (right) Sylgard 184 substrates at 30% applied strain (ϵ_{appl}). b) The corresponding FEA results. c) Line scans along a straight segment of a serpentine interconnect (location indicated by the dashed white lines in (a) and (b)).

occurs in the serpentes, thereby enhancing their stretchability. We also outline the dependence of the stretchability on the material selected for the substrates and interconnects. FEA

simulations indicate that the elastic stretchability increases with decreasing modulus of both the substrate and the interconnect due to the corresponding decreased bending stiffness. The

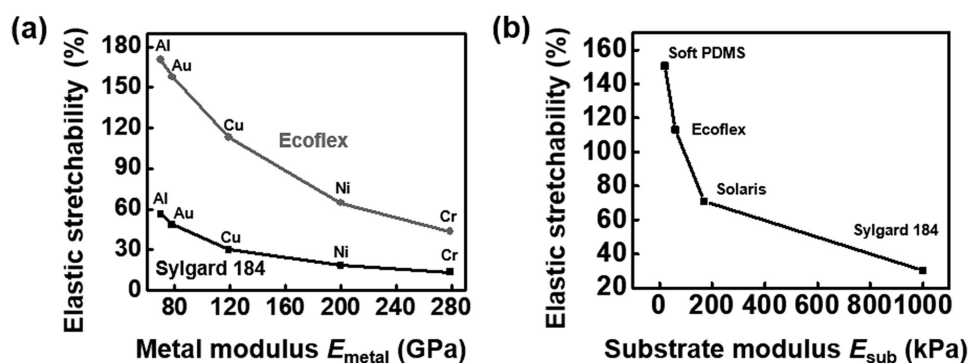


Figure 5. a) The elastic stretchability of a metallic serpentine interconnect on a 5 μm thick substrate (Ecoflex and Sylgard 184) as a function of the elastic modulus of the metallic interconnect. b) The elastic stretchability of a copper serpentine interconnect on a 5 μm thick substrate as a function of the elastic modulus of the substrate.

practical consequence of these ideas is that advanced designs in stretchable electronics might incorporate a packaging strategy in which an outer, passive elastomeric enclosure houses a freely suspended thin substrate to provide protection from the surrounding environment. Owing to the widespread use of serpentine interconnect designs in stretchable electronic systems, we believe this study provides useful design guidelines and insight into producing high-performance electronic devices capable of extreme stretchability.

4. Experimental Section

Finite Element Analysis: The commercial software package ABAQUS^[43] enabled studies of the mechanical response of the serpentine interconnects on elastomers. The elastomeric substrates were modeled by the hexahedron 3D solid element (C3D8R). The serpentine interconnect, which consists of a Ti/SiO₂ adhesion layer, two PI layers, and a Cu layer, was modeled by four-node composite shell elements (S4R). The meshes used in the numerical calculation were refined to ensure accuracy. Displacement boundary conditions were applied to both edges of the substrate to produce uniaxial tension of the substrates.

Fabrication of the Serpentine Interconnects on Silicone Substrates: Spin-casting poly(methyl methacrylate) (PMMA) 495 A8 (MicroChem, Westborough, MA) at 3000 rpm for 30 s and heating on a hot plate at 180 °C for 2 min formed a sacrificial layer on a glass slide. An additional spin-casting of PI (1.2 μm, PI 2545, HD Microsystems, Parlin, NJ) at 4000 rpm for 60 s and baking on a hot plate at 110 °C for 1 min and 150 °C for 5 min produced a bottom encapsulating layer. Heating in a vacuum oven at 250 °C for 75 min cured this layer. Electron beam evaporation (AJA International, Scituate, MA) then created a 100 nm layer of Cu. A second layer of PI (same conditions as above) served as a top encapsulation layer for the Cu. Next, photolithography defined the serpentine layouts: spin-casting AZ 4620 photoresist (MicroChem, Westborough, MA) at 1000 rpm for 60 s, baking at 110 °C for 4 min, UV exposing through an iron oxide mask to 800 mJ cm⁻² (MJB3 Masker Aligner, Suss MicroTec, Garching, Germany), developing in one part AZ 400K developer (MicroChem, Westborough, MA) to three parts deionized water for 2 min, reactive-ion etching (March, Nordson, Carlsbad, CA) at 300 mTorr and 150 W with 20 sccm O₂ gas for 10 min to remove the top PI encapsulant, chemically etching in one part Cu etchant (CE-100, Transene, Danvers, MA) to ten parts deionized water for 10 s to remove the Cu, and reactive-ion etching again (same conditions as above) to remove the bottom PI and PMMA layers. Immersion in hot acetone (65 °C) for 3 h undercut the sacrificial PMMA layer. Water-soluble tape (Aquasol, North Tonawanda, NY) retrieved the samples from the glass slides. An electron beam deposited 3 nm of Ti and 30 nm of SiO₂ onto the backside of the samples for adhesion to the substrates.

Spin-casting at various speeds between 100 and 6000 rpm created silicone substrates with thickness ranging between 7 and 700 μm. Various techniques, including contact profilometry (Sloan Dektak3 ST, Veeco Sloan/Dektak, Oyster Bay, NY), optical profilometry (Nexview 3D optical surface profiler, Zygo, Middlefield, CT), and optical microscopy, allowed for measurement of the thickness of the substrate. For Ecoflex 00-30 (Smooth-On, Macungie, Pennsylvania), mixing the two components in a 1:1 weight ratio followed by curing at room temperature for 4 h produced the substrates. For Sylgard 184 (Dow Corning, Auburn, MI), mixing the components in a 10:1 ratio followed by curing in an oven at 70 °C for 1 h generated the substrates. For thin substrates, trichloro(octadecyl)silane or a release agent (Ease Release 200, Mann, Macungie, Pennsylvania) served as an anti-adhesive layer, which facilitated retrieval of the substrates from the glass slides. Cutting the silicone with a razor while still on the glass slides yielded substrates of the desired areal dimensions. After forming the serpentes (on water-soluble tape) and the substrates, ultraviolet ozone exposure

enabled strong bonding between the two. Subsequent immersion in water removed the tape.

Characterization of the Samples in the SEM, Optical Profiler, and Cyclic Loader: A stiff polymeric frame (with a 1 cm × 1 cm central square hole) coated with Kapton tape (DuPont, Wilmington, DE) retrieved the samples from the glass slides, thus facilitating handling while transferring to the characterization equipment. For experiments requiring prestretching, a homemade uniaxial stretcher stretched the sample to the desired length. A second polymeric frame then retrieved the sample from the stretcher to transfer to the characterization equipment. Due to the relative rigidity of the frames, the samples maintained their stretched configurations during characterization.

An optical microscope, a scanning electron microscope (Hitachi S4800, Tokyo, Japan), and a 3D optical profiler (Nexview 3D optical surface profiler, Zygo, Middlefield, CT) provided images of the serpentes in their un-deformed and deformed states. A homemade cyclic loader with a stepper motor stretched the samples to a displacement specified through a LabVIEW program for 25 000 cycles at 5 Hz. After cycling, optical microscopy assessed the presence or absence of fatigue cracks.

Supporting Information

Supporting Information is available from the Wiley Online Library or from the author.

Acknowledgements

T.P., M.P., and Y.M. contributed equally to this work. T.P. and X.F. acknowledge the support from the National Basic Research Program of China (Grant No. 2015CB351900). T.P. acknowledges the support from Fundamental Research Funds for the Central Universities of China (Grant No. ZYGX2016KYQD132). Y.M. and X.F. acknowledge the support from the National Natural Science Foundation of China (Grant Nos. 11402135 and 11320101001). Y.H. acknowledges the support from the NSF (Grant Nos. DMR-1121262, CMMI-1400169, and CMMI-1534120) and the NIH (Grant No. R01EB019337).

Conflict of Interest

The authors declare no conflict of interest.

Keywords

buckling, flexible electronics, plasticity, serpentine interconnects, stretchable electronics

Received: May 15, 2017
Revised: June 25, 2017
Published online: August 4, 2017

- [1] S. P. Lacour, S. Wagner, Z. Huang, Z. Suo, *Appl. Phys. Lett.* **2003**, *82*, 2404.
- [2] D.-Y. Khang, H. Jiang, Y. Huang, J. A. Rogers, *Science* **2006**, *311*, 208.
- [3] F. Xu, X. Wang, Y. Zhu, Y. Zhu, *Adv. Funct. Mater.* **2012**, *22*, 1279.
- [4] A. Robinson, A. Aziz, Q. Liu, Z. Suo, S. P. Lacour, *J. Appl. Phys.* **2014**, *115*, 143511.
- [5] D.-H. Kim, N. Lu, Y. Huang, J. A. Rogers, *MRS Bull.* **2012**, *37*, 226.

- [6] T. Cheng, Y.-Z. Zhang, W.-Y. Lai, Y. Chen, W.-J. Zeng, W. Huang, *J. Mater. Chem. C* **2014**, 2, 10369.
- [7] H. Li, Y. Xu, X. Li, Y. Chen, Y. Jiang, C. Zhang, B. Lu, J. Wang, Y. Ma, Y. Chen, Y. Huang, M. Ding, H. Su, G. Song, Y. Luo, X. Feng, *Adv. Healthcare Mater.* **2017**, 6, 1601013.
- [8] C. H. Lee, Y. Ma, K.-I. Jang, A. Banks, T. Pan, X. Feng, J. S. Kim, D. Kang, M. S. Raj, B. L. McGrane, B. Morey, X. Wang, R. Ghaffari, Y. Huang, J. A. Rogers, *Adv. Funct. Mater.* **2015**, 25, 3698.
- [9] W. Gao, S. Emaminejad, H. Y. Y. Nyein, S. Challa, K. Chen, A. Peck, H. M. Fahad, H. Ota, H. Shiraki, D. Kiriya, D.-H. Lien, G. A. Brooks, R. W. Davis, A. Javey, *Nature* **2016**, 529, 509.
- [10] A. Chortos, G. I. Koleilat, R. Pfattner, D. Kong, P. Lin, R. Nur, T. Lei, H. Wang, N. Liu, Y.-C. Lai, M.-G. Kim, J. W. Chung, S. Lee, Z. Bao, *Adv. Mater.* **2016**, 28, 4441.
- [11] S. I. Park, D. S. Brenner, G. Shin, C. D. Morgan, B. A. Copits, H. U. Chung, M. Y. Pullen, K. N. Noh, S. Davidson, S. J. Oh, J. Yoon, K.-I. Jang, V. K. Samineni, M. Norman, J. G. Grajales-Reyes, S. K. Vogt, S. S. Sundaram, K. M. Wilson, J. S. Ha, R. Xu, T. Pan, T.-i. Kim, Y. Huang, M. C. Montana, J. P. Golden, M. R. Bruchas, R. W. Gereau Iv, J. A. Rogers, *Nat. Biotechnol.* **2015**, 33, 128.
- [12] M. Kaltenbrunner, T. Sekitani, J. Reeder, T. Yokota, K. Kuribara, T. Tokuhara, M. Drack, R. Schwodiauer, I. Graz, S. Bauer-Gogonea, S. Bauer, T. Someya, *Nature* **2013**, 499, 458.
- [13] J. Kim, M. Lee, H. J. Shim, R. Ghaffari, H. R. Cho, D. Son, Y. H. Jung, M. Soh, C. Choi, S. Jung, K. Chu, D. Jeon, S.-T. Lee, J. H. Kim, S. H. Choi, T. Hyeon, D.-H. Kim, *Nat. Commun.* **2014**, 5, 5747.
- [14] J. Kim, A. Banks, H. Cheng, Z. Xie, S. Xu, K.-I. Jang, J. W. Lee, Z. Liu, P. Gutruf, X. Huang, P. Wei, F. Liu, K. Li, M. Dalal, R. Ghaffari, X. Feng, Y. Huang, S. Gupta, U. Paik, J. A. Rogers, *Small* **2015**, 11, 906.
- [15] T. Someya, T. Sekitani, S. Iba, Y. Kato, H. Kawaguchi, T. Sakurai, *Proc. Natl. Acad. Sci. USA* **2004**, 101, 9966.
- [16] G. Schwartz, B. C. K. Tee, J. Mei, A. L. Appleton, D. H. Kim, H. Wang, Z. Bao, *Nat. Commun.* **2013**, 4, 1859.
- [17] D.-H. Kim, N. Lu, R. Ma, Y.-S. Kim, R.-H. Kim, S. Wang, J. Wu, S. M. Won, H. Tao, A. Islam, K. J. Yu, T.-i. Kim, R. Chowdhury, M. Ying, L. Xu, M. Li, H.-J. Chung, H. Keum, M. McCormick, P. Liu, Y.-W. Zhang, F. G. Omenetto, Y. Huang, T. Coleman, J. A. Rogers, *Science* **2011**, 333, 838.
- [18] J. W. Lee, R. Xu, S. Lee, K.-I. Jang, Y. Yang, A. Banks, K. J. Yu, J. Kim, S. Xu, S. Ma, S. W. Jang, P. Won, Y. Li, B. H. Kim, J. Y. Choe, S. Huh, Y. H. Kwon, Y. Huang, U. Paik, J. A. Rogers, *Proc. Natl. Acad. Sci. USA* **2016**, 113, 6131.
- [19] D.-H. Kim, J. Xiao, J. Song, Y. Huang, J. A. Rogers, *Adv. Mater.* **2010**, 22, 2108.
- [20] Y. Y. Hsu, M. Gonzalez, F. Bossuyt, J. Vanfleteren, I. D. Wolf, *IEEE Trans. Electron Devices* **2011**, 58, 2680.
- [21] M. Gonzalez, F. Axisa, M. V. Bulcke, D. Brosteaux, B. Vandeveld, J. Vanfleteren, *Microelectron. Reliab.* **2008**, 48, 825.
- [22] Y. Zhang, S. Wang, X. Li, J. A. Fan, S. Xu, Y. M. Song, K.-J. Choi, W.-H. Yeo, W. Lee, S. N. Nazaar, B. Lu, L. Yin, K.-C. Hwang, J. A. Rogers, Y. Huang, *Adv. Funct. Mater.* **2014**, 24, 2028.
- [23] T. Li, Z. Suo, S. P. Lacour, S. Wagner, *J. Mater. Res.* **2005**, 20, 3274.
- [24] O. v. d. Sluis, Y. Y. Hsu, P. H. M. Timmermans, M. Gonzalez, J. P. M. Hoefnagels, *J. Phys. D: Appl. Phys.* **2011**, 44, 034008.
- [25] D. S. Gray, J. Tien, C. S. Chen, *Adv. Mater.* **2004**, 16, 393.
- [26] F. Xu, W. Lu, Y. Zhu, *ACS Nano* **2011**, 5, 672.
- [27] T. Cheng, Y. Zhang, W.-Y. Lai, W. Huang, *Adv. Mater.* **2015**, 27, 3349.
- [28] S. Yang, E. Ng, N. Lu, *Extreme Mech. Lett.* **2015**, 2, 37.
- [29] Y. H. Jung, J. Lee, Y. Qiu, N. Cho, S. J. Cho, H. Zhang, S. Lee, T. J. Kim, S. Gong, Z. Ma, *Adv. Funct. Mater.* **2016**, 26, 4618.
- [30] X. Huang, Y. Liu, H. Cheng, W.-J. Shin, J. A. Fan, Z. Liu, C.-J. Lu, G.-W. Kong, K. Chen, D. Patnaik, S.-H. Lee, S. Hage-Ali, Y. Huang, J. A. Rogers, *Adv. Funct. Mater.* **2014**, 24, 3846.
- [31] L. Xu, S. R. Gutbrod, Y. Ma, A. Petrossians, Y. Liu, R. C. Webb, J. A. Fan, Z. Yang, R. Xu, J. J. Whalen, J. D. Weiland, Y. Huang, I. R. Efimov, J. A. Rogers, *Adv. Mater.* **2015**, 27, 1731.
- [32] Y.-Y. Hsu, M. Gonzalez, F. Bossuyt, F. Axisa, J. Vanfleteren, I. De Wolf, *Thin Solid Films* **2011**, 519, 2225.
- [33] D.-H. Kim, N. Lu, R. Ghaffari, Y.-S. Kim, S. P. Lee, L. Xu, J. Wu, R.-H. Kim, J. Song, Z. Liu, J. Viveni, B. de Graff, B. Elolampi, M. Mansour, M. J. Slepian, S. Hwang, J. D. Moss, S.-M. Won, Y. Huang, B. Litt, J. A. Rogers, *Nat. Mater.* **2011**, 10, 316.
- [34] L. Klinker, S. Lee, J. Work, J. Wright, Y. Ma, L. Ptaszek, R. C. Webb, C. Liu, N. Sheth, M. Mansour, J. A. Rogers, Y. Huang, H. Chen, R. Ghaffari, *Extreme Mech. Lett.* **2015**, 3, 45.
- [35] H. C. Ko, M. P. Stoykovich, J. Song, V. Malyarchuk, W. M. Choi, C.-J. Yu, J. B. GeddesIII, J. Xiao, S. Wang, Y. Huang, J. A. Rogers, *Nature* **2008**, 454, 748.
- [36] Y. M. Song, Y. Xie, V. Malyarchuk, J. Xiao, I. Jung, K.-J. Choi, Z. Liu, H. Park, C. Lu, R.-H. Kim, R. Li, K. B. Crozier, Y. Huang, J. A. Rogers, *Nature* **2013**, 497, 95.
- [37] J. A. Fan, W.-H. Yeo, Y. Su, Y. Hattori, W. Lee, S.-Y. Jung, Y. Zhang, Z. Liu, H. Cheng, L. Falgout, M. Bajema, T. Coleman, D. Gregoire, R. J. Larsen, Y. Huang, J. A. Rogers, *Nat. Commun.* **2014**, 5, 3266.
- [38] Y. Su, Z. Liu, S. Wang, R. Ghaffari, D.-H. Kim, K.-C. Hwang, J. A. Rogers, Y. Huang, *Int. J. Solids Struct.* **2014**, 51, 1555.
- [39] I. M. Daniel, O. Ishai, I. M. Daniel, I. Daniel, *Engineering Mechanics of Composite Materials*, Oxford University Press, New York **1994**.
- [40] S. Wang, J. Song, D.-H. Kim, Y. Huang, J. A. Rogers, *Appl. Phys. Lett.* **2008**, 93, 023126.
- [41] H. Jiang, D.-Y. Khang, H. Fei, H. Kim, Y. Huang, J. Xiao, J. A. Rogers, *J. Mech. Phys. Solids* **2008**, 56, 2585.
- [42] J. Song, H. Jiang, Z. J. Liu, D. Y. Khang, Y. Huang, J. A. Rogers, C. Lu, C. G. Koh, *Int. J. Solids Struct.* **2008**, 45, 3107
- [43] *ABAQUS Analysis User's Manual*, Hibbitt, Karlsson & Sorensen, Pawtucket, RI, USA, V6.10 **2010**.